Power Electronic Systems
Laboratory

IEEE Journal of Emerging and Selected Topics in Power Electronics, Vol. 5, No. 3, pp. 1404-1414, September 2017

Electronically Controllable Impedance for Tuning of Active Metamaterials

D. O. Boillat,
T. Friedli,
J. W. Kolar

Eidgenössische Technische Hochschule Zürich
Swiss Federal Institute of Technology Zurich

Electronically Controllable Impedance for Tuning of Active Metamaterials

David O. Boillat*, Thomas Friedli†, and Johann W. Kolar*
* Power Electronic Systems Laboratory (PES), ETH Zurich, 8092 Zurich, Switzerland
† ABB Switzerland Ltd, PG Transportation, 5300 Turgi, Switzerland

***Abstract*— In recent years, passive metamaterials consisting of a geometrical arrangement of LCR-resonator-type base units are proposed for the shielding of magnetic stray fields at low- and medium-frequencies. The screening factor of such passive metamaterial shields can be deteriorated by component value tolerances and variations with temperature and / or by aging. These issues can be overcome with an active metamaterial assembled by an array of engineered active base units. Each base unit contains a LCR-resonator and a control unit called electronically controllable impedance (ECI). The ECI consists of a 4-quadrant power converter with integrated measurement and control units for emulating an arbitrary impedance and is used to tune the LCR-resonator such that the base unit exhibits an ideally purely electric inductive or capacitive behavior when excited by an external field. Thereby, each single LCR-resonator's resonant frequency is tuned to be close to the excitation frequency and the resonator's quality factor Q is optimally adjusted. This paper shows different realizations of an ECI and proposes an ECI control algorithm to tune the resonant frequency and to adjust the quality factor Q of the resonators. Furthermore, experimental verifications of the ECI concept employing a linear power amplifier are provided.**

***Index Terms*—Electronically controllable impedance, electronically controllable admittance, active magnetic field shielding, metamaterial, resonance, electric inductive or capacitive behavior.**

ABBREVIATIONS

CCVS	Current Controlled Voltage Source
DSP	Digital Signal Processor
ECI	Electronically Controllable Impedance
ECA	Electronically Controllable Admittance
ETPRC	Electronically Tuned Parallel Resonant Circuit
ETSRC	Electronically Tuned Series Resonant Circuit
FPGA	Field Programmable Gate Array
PCB	Printed Circuit Board
VCCS	Voltage Controlled Current Source

I. INTRODUCTION

METAMATERIALS belong to an emerging class of artificial materials consisting of geometrical arrangements of engineered base units [1]–[3]. These base units, typically LC-resonators [4], and the interactions among them define the electromagnetic properties of the metamaterial (cf. **Fig. 1**). An adequate design of the base units thus allows achieving electromagnetic effects not commonly found in nature. Examples are a negative real part of the resulting permittivity [5] and / or permeability [4], [6], or a negative [4] or an unusually high [7] real part of the refraction index in a certain frequency range.

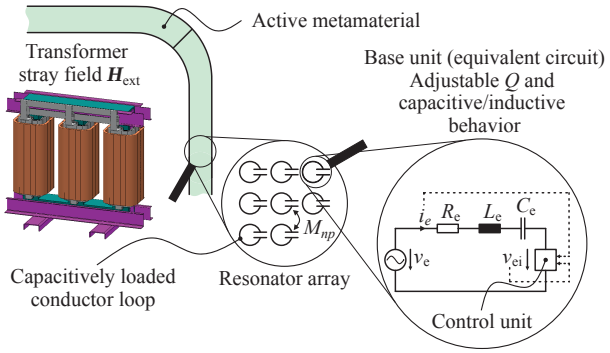

Figure 1: Concept of shielding magnetic fields with an active metamaterial at the example of a medium voltage dry-type distribution transformer from ABB (1 MVA/10 kV (50 Hz); Resibloc [9] – transformer picture taken from [10]).

The word "resulting" is used in the sense that for an incident electromagnetic wave, the metamaterial acts like a compact material having the same permittivity and permeability as the resulting ones. The parameters can be regarded as "resulting" if the wavelength of the incident wave is much larger than the geometrical dimensions of the base units [8].

Metamaterials have been proven to be powerful and flexible to obtain desired electromagnetic properties in the radio and optical frequency ranges (i.e. frequencies $>$ 1 MHz) [8]. Recent publications revealed that the concept of metamaterials can be successfully employed also in applications with much lower working frequencies ($<$ 100 kHz), especially for the shielding of magnetic stray fields [11], [12]. Shielding of magnetic fields is for instance necessary for distribution power transformer stations [13] and power cables in residential areas [11], wireless charging units for electrical vehicles [12], [14], and induction heaters for cooking [15]. All applications making use of the mentioned devices could benefit from a very effective metamaterial shield.

For shielding low-frequency magnetic fields, to the best knowledge of the authors, only passive metamaterials consisting of passive base units have been employed so far [11], [12], [16]. The screening factor of such passive metamaterial shields can be deteriorated by component value tolerances of the base units as well as by variations of the component values with temperature and / or by aging. Moreover, a desired high screening factor may only be achieved with complicated

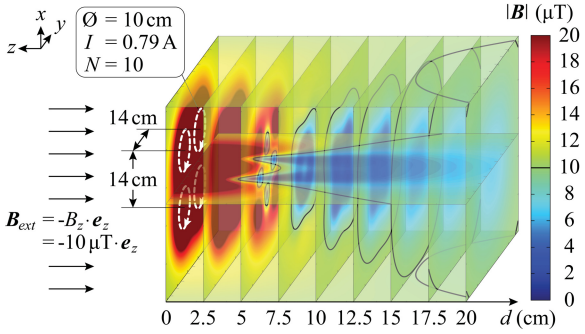

Figure 2: Calculated field shielding capability of a simple metamaterial in the xy-plane built by four identical base units, each one consisting of a circular coil (dashed white lines) with $N = 10$ turns and a diameter of 10 cm. For illustration purpose, the z-axis is scaled up compared to the x-axis and y-axis, which both have the same scale.

structures of the base units. To overcome these issues a novel active base unit and / or active metamaterial, is conceptualized, designed and tested in this paper (cf. Fig. 1).

In order to understand how magnetic fields can be shielded with a metamaterial, first a simplified structure, i.e. a metamaterial in the xy-plane with four identical base units surrounded by air as shown in **Fig. 2** is studied. A base unit consists of a circular coil with N turns and surface area A_c. The coil is terminated by a load impedance $\underline{Z}_\mathrm{l}$ (typically a capacitor, cf. Fig. 1). The metamaterial is exposed to a sinusoidal time-varying, homogenous magnetic field $\boldsymbol{H}_\mathrm{ext} = [0, 0, -H_\mathrm{z} \cdot \cos(\omega_0 t)]^\mathsf{T}$ in negative z-direction with frequency $f_0 = \omega_0/(2\pi)$. To simplify the following analysis, a phasor notation marked by an underline is adopted, i.e. the phasor of $\boldsymbol{H}_\mathrm{ext}$ is $\underline{\boldsymbol{H}}_\mathrm{ext} = \left[\underline{H}_\mathrm{x}, \underline{H}_\mathrm{y}, \underline{H}_\mathrm{z}\right]^\mathsf{T}$ which gives $\underline{\boldsymbol{H}}_\mathrm{ext} = [0, 0, -H_\mathrm{z}]^\mathsf{T}$ for the assumed direction of the magnetic field. Considering only coil 1 for instance, the magnetic flux-density field $\underline{\boldsymbol{B}}_\mathrm{ext} = \left[\underline{B}_\mathrm{x}, \underline{B}_\mathrm{y}, \underline{B}_\mathrm{z}\right]^\mathsf{T} = \mu_0 \cdot \underline{\boldsymbol{H}}_\mathrm{ext} = \mu_0 \cdot [0, 0, -H_\mathrm{z}]^\mathsf{T}$ associated to $\underline{\boldsymbol{H}}_\mathrm{ext}$ induces a voltage $\underline{v}_\mathrm{ind,1}$ in the coil according to Faraday's Law of Induction:

$$\underline{v}_\mathrm{ind,1} = j\omega_0 \cdot N \cdot \underline{B}_\mathrm{z} \cdot A_\mathrm{c}. \tag{1}$$

The induced voltage generates a current $\underline{i}_\mathrm{c}$, with positive direction as indicated in Fig. 2, which is then given by

$$\underline{i}_\mathrm{c,1} = -\frac{\underline{v}_\mathrm{ind,1}}{\underline{Z}_\mathrm{tot}} = -\frac{\underline{v}_\mathrm{ind,1}}{\underline{Z}_\mathrm{c} + \underline{Z}_\mathrm{l}} = -\frac{j\omega_0 \cdot N \cdot \underline{B}_\mathrm{z} \cdot A_\mathrm{c}}{\underline{Z}_\mathrm{c} + \underline{Z}_\mathrm{l}}, \tag{2}$$

where $\underline{Z}_\mathrm{c}$ is the impedance of the coil. This current $\underline{i}_\mathrm{c,1}$ evokes a magnetic field $\underline{\boldsymbol{H}}_\mathrm{c,1}$ with $|\boldsymbol{H}_\mathrm{c,1}| \sim i_\mathrm{c,1}$ and hence a flux-density $\underline{\boldsymbol{B}}_\mathrm{c,1} = \mu_0 \cdot \underline{\boldsymbol{H}}_\mathrm{c,1}$.

As just explained for coil 1, currents $\underline{i}_{\mathrm{c},k}$ ($k = 2, 3, 4$) are also induced in the three other coils. These currents generate magnetic flux-densities $\underline{\boldsymbol{B}}_{\mathrm{c},k}$ which are then also inducing voltages in coil 1. This effect can be modeled considering the magnetic coupling and / or mutual inductances between the coils. Because of the homogeneous external field and the coil arrangement showing mirror symmetry along the x-axis and y-axis, the finally occurring currents in all four coils are identical and hence (2) changes to

$$\underline{i}_{\mathrm{c},k} = -\frac{j\omega_0 \cdot N \cdot \underline{B}_\mathrm{z} \cdot A_\mathrm{c}}{\underline{Z}_\mathrm{tot} - j\omega_0 \cdot (2M_{1,2} + M_{1,3})} = -\frac{j\omega_0 \cdot N \cdot \underline{B}_\mathrm{z} \cdot A_\mathrm{c}}{\underline{Z}_\mathrm{tot,4}}. \tag{3}$$

$M_{n,p}$ is the mutual inductance between coils n and p ($n \neq p$).

In order to be able to lower $\underline{\boldsymbol{B}}_\mathrm{ext}$ in magnitude, i.e. to achieve a shielding effect, the total field

$$\underline{\boldsymbol{B}}_\mathrm{c,tot} = \sum_{k=1}^{4} \underline{\boldsymbol{B}}_\mathrm{c,k} \tag{4}$$

generated by the induced coil currents $\underline{i}_{\mathrm{c},k}$ given in (3) needs to oppose $\underline{\boldsymbol{B}}_\mathrm{ext}$. This is achieved if $\underline{Z}_\mathrm{tot,4}$ at f_0 is purely inductive [11], i.e. $\underline{Z}_\mathrm{tot,4} = j\omega_0 \cdot L_\mathrm{d}$, which results according to (3) in

$$\underline{i}_{\mathrm{c},k} = -\frac{j\omega_0 \cdot N \cdot \underline{B}_\mathrm{z} \cdot A_\mathrm{c}}{j\omega_0 \cdot L_\mathrm{d}} = \frac{N \cdot B_\mathrm{z} \cdot A_\mathrm{c}}{L_\mathrm{d}}, \tag{5}$$

where $B_\mathrm{z} = \mu_0 \cdot H_\mathrm{z}$. Intuitively, this can be understood by considering $\underline{\boldsymbol{B}}_\mathrm{c,tot}$ in the xy-plane for $z = 0$, where $\underline{\boldsymbol{B}}_\mathrm{c,tot}$ has only a z-component. For $\underline{Z}_\mathrm{tot,4} = j\omega_0 \cdot L_\mathrm{d}$ positive currents result, cf. (5), which are inside the coils opposing the external field, cf. Fig. 2. If the coils are in close proximity to each other, $\underline{\boldsymbol{B}}_\mathrm{c,tot}$ is predominately in opposite direction to $\underline{\boldsymbol{B}}_\mathrm{ext}$.

The field shielding capability of the metamaterial for $f_0 =$ 1 kHz, $B_\mathrm{z} = 10$ μT (i.e. $\boldsymbol{B}_\mathrm{ext} = [0, 0, -10\ \mu\mathrm{T} \cdot \cos(2\pi f_0 t)]^\mathsf{T}$) and coils with $N = 10$ turns and a diameter of 10 cm is demonstrated in Fig. 2 for time $t = 0$. The field strength of $|\boldsymbol{B}_\mathrm{tot}| = 10$ μT is highlighted with black lines. Only the field magnitude distribution for $z < 0$ is given, because the distribution is mirror-symmetrical with respect to the xy-plane. A total impedance of $\underline{Z}_\mathrm{tot,4} = j\omega_0 \cdot L_\mathrm{d}$ with $L_\mathrm{d} = 1$ μH is assumed, which leads then to $\underline{i}_{\mathrm{c},k} = 0.79$ A according to (5). Starting from a distance of $d = 7.5$ cm behind the metamaterial (negative z-direction), the magnitude of the total magnetic flux-density field $\boldsymbol{B}_\mathrm{tot} = \boldsymbol{B}_\mathrm{ext} + \boldsymbol{B}_\mathrm{c,tot}$ is reduced compared to $|\boldsymbol{B}_\mathrm{ext}| = B_\mathrm{z} = 10$ μT. The field strength of $|\boldsymbol{B}_\mathrm{tot}| = 10$ μT is highlighted with black lines in Fig. 2.

It is noted that if $\underline{Z}_\mathrm{tot,4}$ at f_0 is purely capacitive, the external field is enhanced which can be exploited to increase wireless power transfers [8].

Typically, in a passive metamaterial as for instant analyzed in [11], each coil in Fig. 1 is loaded by a capacitor, i.e. $\underline{Z}_\mathrm{l} = 1/(j\omega_0 \cdot C_\mathrm{l})$. Considering the resistive parts R_cl of the coil and of C_l, the base unit can thus be modeled by an LCR-resonant circuit with total impedance

$$\underline{Z}_\mathrm{tot} = R_\mathrm{cl} + j\omega_0 \cdot L_\mathrm{c} + 1/(j\omega_0 \cdot C_\mathrm{l}), \tag{6}$$

where L_c is the self-inductance of the coil. In this case, the current of coil 1 for example results according to (3) in

$$\underline{i}_\mathrm{c,1} = -\frac{j\omega_0 \cdot \underline{B}_\mathrm{z} \cdot A_\mathrm{c} \cdot N}{R_\mathrm{cl} + j\omega_0 \cdot (L_\mathrm{c} - 2M_{1,2} - M_{1,3}) + 1/(j\omega_0 \cdot C_\mathrm{l})}. \tag{7}$$

In order to shield the external magnetic field, first, the magnitude of $\underline{Z}_\mathrm{tot,4} = R_\mathrm{cl} + j\omega_0 \cdot (L_\mathrm{c} - 2M_{1,2} - M_{1,3}) + 1/(j\omega_0 \cdot C_\mathrm{l})$ at f_0 should be small enough, such that the field generated by the inducted current has a significant impact on the external

field. And second, the phase of $\underline{Z}_{\text{tot},4}$ at f_0 needs to be 90° (inductive behavior). Accordingly, the base unit is designed such that it achieves a sufficiently high quality factor Q and that the frequency of the resonance between $(L_\text{c} - 2M_{1,2} - M_{1,3})$ and C_l is just slightly below the exciting frequency f_0 of the external field (i.e. over-resonant operation of the base unit). Typically, R_cl prevents the base unit to achieve the two mentioned requirements at the same time and tolerances of the component values make it cumbersome to exactly tune the base unit to the desired frequency slightly higher than f_0.

An active load $\underline{Z}_\text{l}$, which can adjust its impedance in all four quadrants of the complex plane, would be able to compensate R_cl and to adjust ideally a purely inductive behavior of $\underline{Z}_{\text{tot},4}$. Such an active load can consists of a capacitor and a control unit (Fig. 1) and leads to an active base unit and / or active metamaterial. The concept of an active metamaterial is given in Fig. 1.

Accordingly, this paper focuses on the essential part of an active metamaterial, which is the realization, the control, and the implementation of an active base unit and extends initial investigations of the authors presented in [17]. In order to be active, the base unit needs to incorporate a control unit (cf. Fig. 1) called Electronically Controllable Impedance (ECI) in the following. The concept of an ECI is explained in **Section II**. Two basic options to realize the active base unit integrating an ECI, the electronically tuned series and parallel resonant circuit ETSRC and ETPRC respectively, are investigated. This work revises the properties of the ETSRC derived in [17] and extents the theoretical analysis to the ETPRC. In **Section III**, a possible control algorithm, which is implemented on the ECI, is introduced and analyzed by simulations for the ETSRC and ETPRC. Moreover, the advantages and disadvantages of the two realization options for the active base unit are discussed. A hardware prototype and extensive measurements are shown in **Section IV** for a proof-of-concept ECI embedded in a ETSRC. The paper concludes with **Section V**.

II. Electronically Controllable Impedance

An active base unit is obtained if a control unit called Electronically Controllable Impedance (ECI) is added to the passive base unit consisting of an LCR-resonant circuit (cf. Figs. 1 and **3**). For the following analysis, the equivalent circuits shown in Fig. 3 are employed, whose components are related to the ones employed in Eqs. (6) and (7) by

$$\underline{v}_\text{e} = \underline{v}_\text{ind}, \quad \underline{i}_\text{e} = \underline{i}_\text{c}, \tag{8}$$

$$L_\text{e} = L_\text{c} - 2M_{1,2} - M_{1,3}, \quad C_\text{e} = C_\text{l}, \quad R_\text{e} = R_\text{cl}. \tag{9}$$

With this definitions and because of the negative sign in (2), the equivalent circuits in Fig. 3 need to emulate an electric capacitive behavior (i.e. v_e is lagging i_e) in order to shield the magnetic field. This is considered for the rest of the paper. Typically, an active metamaterial would consist of more than four coils. This can be taken into account by including the mutual coupling of the other additional coils in (9).

The conceptual idea of an ECI is to electronically emulate an impedance in all four quadrants of the complex impedance plane. Four-quadrant operation is required, as it may be possible that the ECI needs to deliver or absorb active and / or reactive power. This can be achieved by a Voltage Controlled Current Source (VCCS) or a Current Controlled Voltage Source (CCVS) with adequate control and measurement devices for delivery and absorption of active as well as reactive power. In the case of a CCVS, if the emulated impedance is $\underline{Z}_\text{ei} := z_\text{ei} \cdot e^{j\Delta\phi_\text{ei}}$, the voltage generated by the source is

$$v_\text{ei}(t) = \hat{i}_\text{e} \cdot z_\text{ei} \cdot \sin\left(\omega_\text{e} t + \Delta\phi_\text{ei}\right), \tag{10}$$

where $\hat{i}_\text{e}$ is the amplitude and $\omega_\text{e} t = \phi_\text{ie}$ denotes the phase of the current i_e with respect to a reference frame. In (10), as below, it is assumed that the excitation v_e is sinusoidal with only one frequency component at f_e.

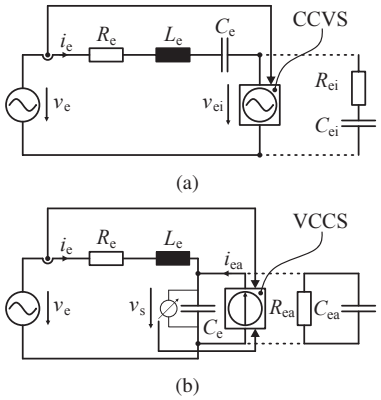

Figure 3: Electronically tuned (a) series and (b) parallel resonant circuit.

There are two main possibilities of combining the ECI with the LCR-resonant circuit, which are depicted in Fig. 3. Seen from the controlled source, a series resonant circuit is shown in **Fig. 3(a)** and a parallel resonant circuit in **Fig. 3(b)**. The impedance of the LCR circuit is given at a certain angular frequency ω by

$$\underline{Z}_\text{e}(\omega) = R_\text{e} + j\omega L_\text{e} + \frac{1}{j\omega C_\text{e}}. \tag{11}$$

R_e is in relation to the damping factor $\delta = \frac{1}{2}\frac{R_\text{e}}{L_\text{e}}$ of the circuit, while L_e as well as C_e determine the self-resonant frequency ($f_\text{self} = \frac{1}{2\pi\sqrt{L_\text{e} \cdot C_\text{e}}}$) of the same circuit. The quality factor Q at a certain angular frequency ω is related to the decay factor δ over

$$Q := \frac{\omega_\text{self}}{2\delta}. \tag{12}$$

In order to obtain, ideally, an infinitely high quality factor Q at a given frequency f_e, it is required that

1) the damping factor δ of the resonant circuit should be decreased (ideally to zero), and
2) the resonant frequency f_res of the resulting circuit (Fig. 3) should be tuned to the excitation frequency.

Due to the ECI's ability to tune the entire impedance of the series resonant circuit, the circuit of Fig. 3(a) is named Electronically Tuned Series Resonant Circuit (ETSRC) in the

following. Similar thoughts apply to the circuit of Fig. 3(b). Correspondingly, the circuit is called Electronically Tuned Parallel Resonant Circuit (ETPRC). The reasons are given below and first explained for the ETSRC.

A. Electronically Tuned Series Resonant Circuit

By adding an ECI $\underline{Z}_{\mathrm{ei}}$ [as for instance schematically depicted in Fig. 3(a)] to the circuit, the total impedance $\underline{Z}_{\mathrm{tot}} = \underline{Z}_{\mathrm{e}} + \underline{Z}_{\mathrm{ei}}$ can be varied in such a way that the two requirements can be fulfilled as briefly demonstrated below. A possible circuit model of the ECI consists of series $C_{\mathrm{ei}}R_{\mathrm{ei}}$-branch as shown in Fig. 3(a). In this case, the decay factor δ_0 and the resonant angular frequency ω_{res} are given to

$$\delta_0 = \frac{1}{2}\frac{R_{\mathrm{e}} + R_{\mathrm{ei}}}{L_{\mathrm{e}}}, \tag{13}$$

$$\omega_{\mathrm{res}} = \sqrt{\omega_{\mathrm{res,t}}^2 - \delta_0^2} = \sqrt{\frac{1}{C_{\mathrm{t}}L_{\mathrm{e}}} - \frac{1}{4}\frac{(R_{\mathrm{e}} + R_{\mathrm{ei}})^2}{L_{\mathrm{e}}^2}}, \tag{14}$$

where $C_{\mathrm{t}} = \frac{C_{\mathrm{e}}C_{\mathrm{ei}}}{C_{\mathrm{e}}+C_{\mathrm{ei}}}$. For $Q \to \infty$, the resistance R_{ei} and the capacitance C_{ei} result in

$$R_{\mathrm{ei,opt.}} = -R_{\mathrm{e}}, \tag{15}$$

$$C_{\mathrm{ei,opt.}} = \frac{C_{\mathrm{e}}}{\omega_{\mathrm{e}}^2 L_{\mathrm{e}}C_{\mathrm{e}} - 1}. \tag{16}$$

It can be seen from the equation above that the resistance R_{ei} is negative in order to compensate the resistance R_{e} inherently present in the circuit. The system's damping is accordingly reduced by R_{ei}, which allows the first requirement to be fulfilled. C_{ei} enables to shift the resonant frequency of the entire circuit to the one of the excitation. Thus, the second requirement can be satisfied. In summary, considering Fig. 3(a), the real part of the impedance $\underline{Z}_{\mathrm{ei}}$ is related to the damping and the imaginary part of it to the tuning of the resonant frequency.

A typical plot of allowable impedance values of $\underline{Z}_{\mathrm{ei}}$ in the complex plane is given in **Fig. 4**. If the real part of the impedance is smaller than $-R_{\mathrm{e}}$, the circuit is unstable, as the damping factor is negative. The signs of the resistance R_{ei} and capacitance C_{ei} are indicated in the figure for all four quadrants. $C_{\mathrm{ei,opt}}$, according to (16), can either be positive or negative depending on whether $\omega_{\mathrm{e}}^2 L_{\mathrm{e}}C_{\mathrm{e}} > 1$ or $\omega_{\mathrm{e}}^2 L_{\mathrm{e}}C_{\mathrm{e}} < 1$. In Fig. 4 a negative $C_{\mathrm{ei,opt}}$ is assumed ($\omega_{\mathrm{e}}^2 L_{\mathrm{e}}C_{\mathrm{e}} < 1$) as it results for the specifications of the prototype given in Table I because of $f_{\mathrm{self}} > f_{\mathrm{e}}$. The borderlines are given by the maximal admissible magnitude $z_{\mathrm{ei,max}}$ of the impedance $\underline{Z}_{\mathrm{ei}}$, by the stability limit and by the maximal allowable voltage or current amplitude, $\hat{v}_{\mathrm{ei,max}}$ or $\hat{i}_{\mathrm{e,max}}$. The voltage or current limit applies first, depending on the desired operating point of the resonant circuit. The maximal impedance magnitude $z_{\mathrm{ei,max}}$ is not a strong criteria, as for large values of z_{ei} the voltage amplitude $\hat{v}_{\mathrm{ei}}$ converges to the one of the excitation $\hat{v}_{\mathrm{e}}$.

B. Electronically Tuned Parallel Resonant Circuit

For the ETPRC [Fig. 3(b)], the ECI is preferentially represented by the admittance $\underline{Y}_{\mathrm{ea}} := y_{\mathrm{ea}} \cdot e^{j\Delta\varphi_{\mathrm{ea}}} = 1/\underline{Z}_{\mathrm{ei}}$, because the ECI emulates a VCCS. Consequently, the admittance $\underline{Y}_{\mathrm{ea}}$

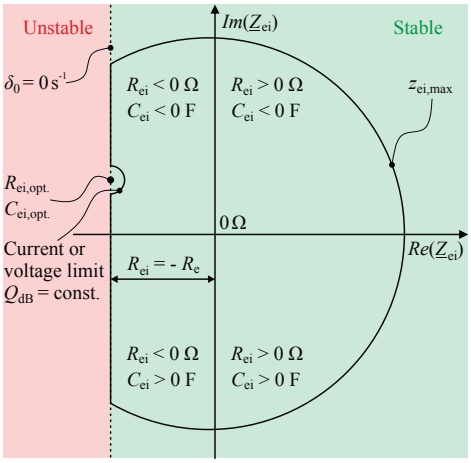

Figure 4: Typical operating area in the complex impedance plane of an electronically controllable impedance $\underline{Z}_{\mathrm{ei}}$ (ETSRC) assuming a negative $C_{\mathrm{ei,opt}}$ (as it is the case for the prototype's specifications given in Table I).

is called Electronically Controllable Admittance (ECA). In this case the adjusting current i_{ea} is given by

$$i_{\mathrm{ea}}(t) = \hat{v}_{\mathrm{s}} \cdot y_{\mathrm{ea}} \cdot \sin\left(\omega_{\mathrm{s}}t + \Delta\varphi_{\mathrm{ea}}\right), \tag{17}$$

where $\omega_{\mathrm{s}}t = \phi_{\mathrm{vs}}$ is the phase of the voltage v_{s}.

A circuit model of the ECA is depicted in Fig. 3(b) and consists of a parallel $R_{\mathrm{ea}}C_{\mathrm{ea}}$-branch. In the following, $\underline{Y}_{\mathrm{ea}} = G_{\mathrm{ea}} + jB_{\mathrm{ea}}$ is represented by its conductance $G_{\mathrm{ea}} = 1/R_{\mathrm{ea}}$ and susceptance $B_{\mathrm{ea}} = \omega_{\mathrm{e}}C_{\mathrm{ea}}$. The damping factor δ_0 and the self-resonant rotational frequency ω_{self} are then given to

$$\delta_0 = \frac{1}{2}\left(\frac{R_{\mathrm{e}}}{L_{\mathrm{e}}} + \frac{G_{\mathrm{ea}}}{C_{\mathrm{e}} + B_{\mathrm{ea}}/\omega_{\mathrm{e}}}\right) = \frac{1}{2}\frac{L_{\mathrm{e}} + R_{\mathrm{e}}R_{\mathrm{ea}}\left(C_{\mathrm{e}} + C_{\mathrm{ea}}\right)}{L_{\mathrm{e}}R_{\mathrm{ea}}\left(C_{\mathrm{e}} + C_{\mathrm{ea}}\right)}, \tag{18}$$

$$\omega_{\mathrm{self}} := \sqrt{\omega_0^2 - \delta_0^2} = \sqrt{\frac{1 + R_{\mathrm{e}}G_{\mathrm{ea}}}{L_{\mathrm{e}}(C_{\mathrm{e}} + B_{\mathrm{ea}}/\omega_{\mathrm{e}})} - \delta_0^2}$$

$$= \sqrt{\frac{R_{\mathrm{e}} + R_{\mathrm{ea}}}{L_{\mathrm{e}}R_{\mathrm{ea}}\left(C_{\mathrm{e}} + C_{\mathrm{ea}}\right)} - \delta_0^2}. \tag{19}$$

To reach $Q \to \infty$ for the ETPRC, the resistance R_{ea} and capacitance C_{ea} result in

$$R_{\mathrm{ea,opt.}} = -\frac{R_{\mathrm{e}}^2 + \omega_{\mathrm{e}}^2 L_{\mathrm{e}}^2}{R_{\mathrm{e}}}, \tag{20}$$

$$C_{\mathrm{ea,opt.}} = \frac{L_e}{R_{\mathrm{e}}^2 + \omega_{\mathrm{e}}^2 L_{\mathrm{e}}^2} - C_{\mathrm{e}}. \tag{21}$$

From the above equations it can be deduced that R_{ea} is negative in order to reduce the damping in the ETPRC and that C_{ea} is positive or negative dependent on the shift of the resonant frequency. If the self-resonant frequency $f_{\mathrm{self,e}} = 1/(2\pi\sqrt{L_{\mathrm{e}} \cdot C_{\mathrm{e}}})$ is greater than the frequency at which the ETPRC should be close to resonance, the capacitance C_{ea} is positive. In the opposite case, C_{ea} is negative. A typical operating area of the ECA in the complex admittance plane is shown in **Fig. 5** for a positive C_{ea} as it would result from the parameter values of the resonant circuit and excitation

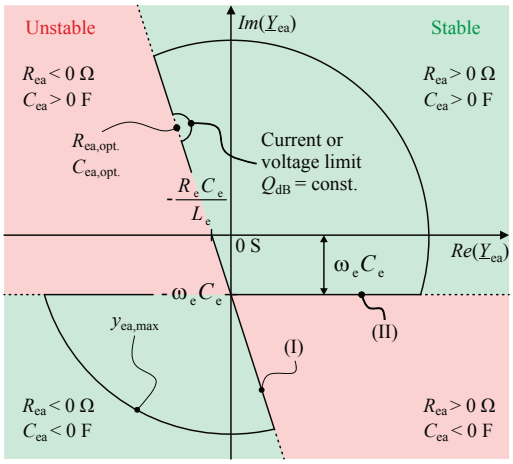

Figure 5: Typical operating area in the complex admittance plane of an electronically controllable admittance $\underline{Y}_{\text{ea}}$ (ETPRC) assuming a positive $C_{\text{ca,opt}}$ (as it would result for the parameter values of the resonant circuit and excitation frequency given in Table I).

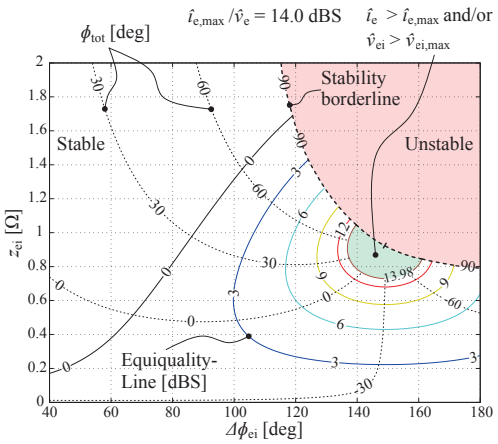

Figure 6: Steady-state quality factor Q_{dB} plotted over the phase $\Delta\phi_{\text{ei}}$ and the magnitude z_{ei} of the ECI $\underline{Z}_{\text{ei}}$ (the phase ϕ_{tot} of $\underline{Z}_{\text{tot}} = \underline{Z}_{\text{e}} + \underline{Z}_{\text{ei}}$ is also given in the plot) [ETSRC].

frequency given in Table I. The signs of the resistance R_{ea} and capacitance C_{ea} are indicated in the figure for all four quadrants.

The borderlines in Fig. 5 are: first, the maximal admissible magnitude $y_{\text{ea,max}}$ of the admittance $\underline{Y}_{\text{ea}}$ in order to not exceed maximal amplitude $\hat{i}_{\text{ea,max}}$ of the current deliverable by the ECA. Second, the maximal allowable voltage amplitude $\hat{v}_{\text{s,max}}$ across the VCCS or amplitude $\hat{i}_{\text{e,max}}$ of the current through the resonant elements. And third, two stability limits (I) and (II), whose derivation is explained in the following. The linear slope (I) results by equating (18) to zero resulting in

$$\begin{aligned} B_{\text{ea}} = Im(\underline{Y}_{\text{ea}}) &= -\frac{\omega_{\text{e}} L_{\text{e}}}{R_{\text{e}}} G_{\text{ea}} - \omega_e C_{\text{e}} \\ &= -\frac{\omega_{\text{e}} L_{\text{e}}}{R_{\text{e}}} Re(\underline{Y}_{\text{ea}}) - \omega_e C_{\text{e}}. \end{aligned} \tag{22}$$

It is noted that the point in the complex admittance plane given by $R_{\text{ea,opt}}$ and $C_{\text{ea,opt}}$ [cf. (20) and (21)] lies on (I). Stability borderline (II) relates to the change of sign in $C_{\text{e}} + B_{\text{ea}}/\omega_{\text{e}}$ for a fixed G_{ea}. If the sign of $C_{\text{e}} + B_{\text{ea}}/\omega_{\text{e}}$ changes also the second summand $G_{\text{ea}}/(C_{\text{e}} + B_{\text{ea}}/\omega_{\text{e}})$ in (18) changes its sign which leads also to a sign change in δ_0 because $\lim_{B_{\text{ea}} \to -\omega_{\text{e}} C_{\text{e}}^{\pm}} (C_{\text{e}} + B_{\text{ea}}/\omega_{\text{e}}) \to \pm\infty$. Accordingly, it follows that (II) is given by

$$B_{\text{ea}} = Im(\underline{Y}_{\text{ea}}) = -\omega_{\text{e}} C_{\text{e}}. \tag{23}$$

The stable, i.e. $\delta_0 > 0$, and unstable, i.e. $\delta_0 < 0$, areas in the complex admittance plane are highlighted in Fig. 5 in green and red, respectively.

III. ECI Control Algorithms and Simulations

Variations in the excitation frequency f_{e} can lead to changes in the values of the capacitance C_{e} and inductance L_{e}. In addition, the resistance R_{e} and the parasitic resistances of C_{e} and L_{e} or the mentioned components themselves may vary with temperature. Furthermore, tolerances in the values of the components may make it difficult to reach the desired Q-factor. To overcome these limitations, this section presents a control algorithm which is able to obtain and keep a certain quality factor Q, despite varying parameters.

Changes in the component values resulting from temperature variations occur within the order of seconds. Thus, the control algorithm needs to be "fast enough" to follow these component variations. Alteration of the excitation frequency could occur during electrical dynamic transients in the device to shield, but are not considered as prevalent.

The quality factor Q_{dB} is in this paper defined as

$$Q_{\text{dB}} := 20 \cdot \log_{10}\left(\frac{\hat{i}_{\text{e}}}{\hat{v}_{\text{e}}}\right). \tag{24}$$

The unit of Q_{dB} is dBS (decibel Siemens). There are two main reasons for introducing this new definition. Firstly, a direct relation between the quality factor Q_{dB} and the current, which is the magnetic field constituent quantity, is obtained. Secondly, the decay factor in (12) can be dependent on the capacitance C_{ei} as well as on the resistance R_{ei}. This is not the case for the ETSRC but for the ETPRC [$\underline{Z}_{\text{ei}}$ can be modeled with a parallel $C_{\text{ei}}R_{\text{ei}}$-branch, cf. Fig. 3(b)]. Variations of C_{ei} and R_{ei} may lead to very low damped eigenmodi at different frequencies than f_{e}. Nevertheless, these eigenmodi show "high" conventional quality factors Q (12) [even though the current amplitude $\hat{i}_{\text{e}}$ is "low"], which makes a clear illustration difficult.

A. Electronically Tuned Series Resonant Circuit

The calculated steady-state quality factor Q_{dB} is plotted in **Fig. 6** as a function of the ECI $\underline{Z}_{\text{ei}} = z_{\text{ei}} \cdot e^{j\Delta\phi_{\text{ei}}}$ for the parameters given in **Table I**. Considering Fig. 6, the maximum current $i_{\text{e,max}}$ through and / or voltage $v_{\text{ei,max}}$ across the ECI is exceeded in the green shaded area. Unstable operation would occur in the read shaded area. Different values of the quality factor a marked with separate colors. The lines with the same

Table I: Specifications of the prototype (the subscript "meas" indicates a measured quantity; for the simulations the calculated quantities were used) [ETSRC].

Circuit	ETSRC	CCVS	Operational amplifier
R_e	0.8 Ω	$\hat{i}_{out,max}$	10 A*
$R_{e,meas}$	0.7 Ω		
L_e	360.0 µH	$\hat{i}_{e,max}$	5 A
$L_{e,meas}$	366.2 µH		
C_e	58.2 µF	$\hat{v}_{ei,max}$	30 V*
$C_{e,meas}$	58.4 µF		
f_{self}	1.1 kHz	$f_{out,max}$	100 kHz*
$f_{self,meas}$	1.088 kHz		
Weight	815 g	Logic	DSP, FPGA
Length	96 mm	Excitation	Voltage v_e
Width	96 mm	Excitation waveform	Sine
Height	111 mm	$\hat{v}_e$	1.0 V
Volume	1 dm^3	f_e	1.0 kHz

*: Not simultaneously (thermal limitation; max. losses of $P_{d,max} = 44$ W)

quality factor are called equiquality-lines. In addition to the equiquality-lines, the phase of the impedance $\underline{Z}_{tot}$ is also depicted in the figure. It can be seen from Fig. 6 that the maximum quality factor $Q_{dB,max}$ is limited by the maximum current or voltage amplitude, for which the ECI is designed. However, along the line with $Q_{dB,max}$, different phases ϕ_{tot} of the total impedance $\underline{Z}_{tot}$ are obtained. Both, $\phi_{tot} = -90°$ and $\phi_{tot} = 90°$ can be reached. In the former case, the ETSRC acts like a capacitor (v_e lags i_e) and in the latter one like an inductor (i_e lags v_e). As mentioned in Section II, a electric capacitive behavior of the base unit is required in order to shield the magnetic stray field.

The closer an operating point is located to the stability border (dashed line in Fig. 6) the less changes in the impedance $\underline{Z}_{ei}$ are damped and consequently the longer it takes to reach a quasi-steady state. Thus, an operation at the stability border is not reasonable. This means that a certain stability margin needs to be considered, which rejects a purely capacitive / inductive behavior of the ETSRC.

A flow chart of the control algorithm is shown in **Fig. 7**. The voltage $v_{ei}(t)$ is applied to the resonant circuit as given by (10). Therefore, one task could be the maximization of the quality factor Q_{dB}. This comprises to find the magnitude z_{ei} and the phase $\Delta\phi_{ei}$ in such a way that the current amplitude $\hat{i}_e$ [Eq. (24)] is maximized (along with the indicated limitations). Firstly, an appropriate starting point is selected based on the measured circuit parameters (A). A point consists of two values, z_{ei} and $\Delta\phi_{ei}$. Then, the magnitude z_{ei}, which leads to the highest possible Q_{dB}-factor for a fixed $\Delta\phi_{ei}$, is adjusted (in discrete steps δz_{ei}) by measuring the current amplitude $\hat{i}_e$ and comparing it with previous values. If this point is found, the phase $\Delta\phi_{ei}$ is increased in the right direction by one step $\delta\Delta\phi_{ei}$ and the magnitude z_{ei} is again selected such that the highest Q_{dB} results. This sequence is repeated until the previously mentioned current or voltage limit is reached (B). In a next step, the capacitive or inductive behavior of the ETSRC is adjusted. As the damping can be further reduced by this adjustment, it is meaningful to decrease the step sizes

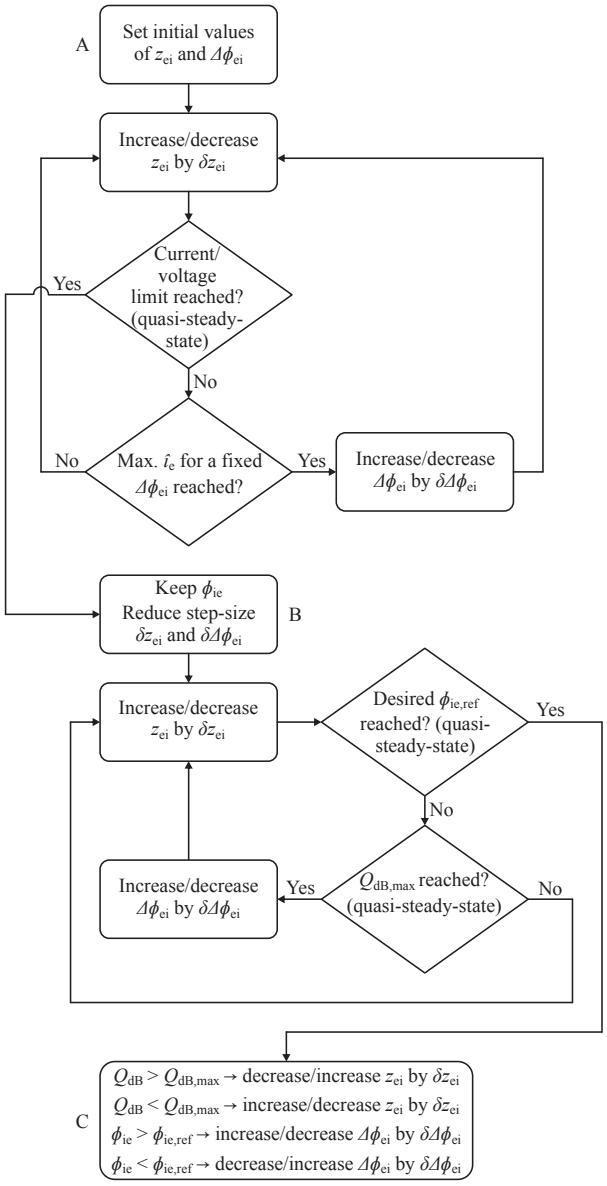

Figure 7: Flow chart of the control algorithm implemented on the ECI (starting point for the control algorithm's path in Fig. 8 is $z_{ei} = 0.1\ \Omega$ and $\Delta\phi_{ei} = 100°$; A, B, C refer to Fig. 8 and Fig. 16) [ETSRC].

δz_{ei} and $\delta\Delta\phi_{ei}$. When the current or voltage limit is reached, the phase ϕ_{ie} of the current i_e (with respect to a reference frame) is locked. This allows the phase to be shifted by the required amount (ϕ_{ie} is an effigy of ϕ_{tot}). The tuning of the ECI $\underline{Z}_{ei}$ in this loop is done in the same way as described above. Once the current-phase ϕ_{ei} has reached the desired value $\phi_{ei,ref}$, the algorithm remains in the attained operating point (C). However, it still keeps controlling the magnitude z_{ei} and phase $\Delta\phi_{ei}$ in the described manner.

For the control algorithm in Fig. 7 the prior knowledge about the component values of the resonant circuit can be used to reach point (C) rapidly: for $f_e < f_{self}$, $\Delta\phi_{ei}$ can be increased while for $f_e > f_{self}$ it can be decreased. Once point

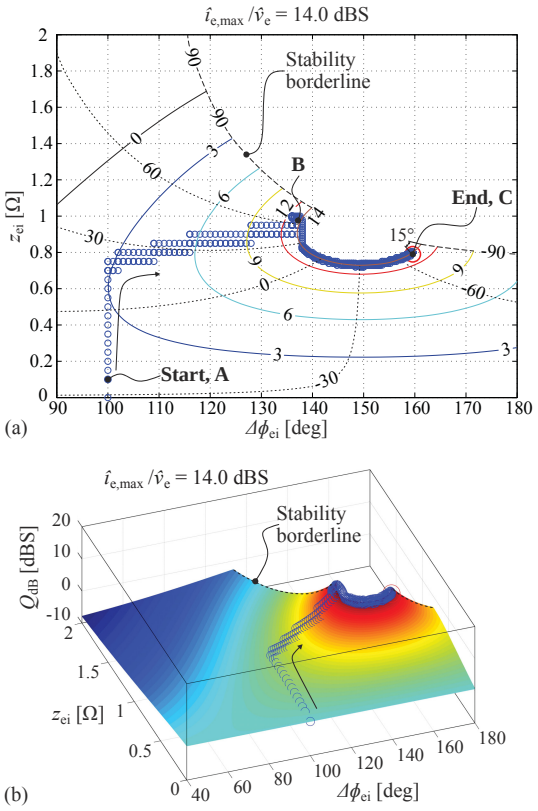

Figure 8: (a) 2D and (b) 3D plot of the control algorithm's path (blue circles) in the $\Delta\phi_{ei}$-z_{ei}-plane (emulated capacitive behavior, ETSRC). Different values of the quality factor a marked with separate colors in (a).

(C) is reached, both z_{ei} and $\Delta\phi_{ei}$ are independently increased or decreased, if needed, such that the desired $Q_{dB,max}$ and $\phi_{ie,ref}$ are obtained. It should be noted that the presented control algorithm is one of many options. In addition, instead of measuring the phase ϕ_{ie} of the current i_e and shifting the phase of the voltage v_{ei} by $\Delta\phi_{ei}$, it would be possible to replace $\Delta\phi_{ei}$ by a delay $T_{d,ei}$, by which the voltage $v_{ei}(t)$ is retarded with respect to the current $i_e(t)$. This may be advantageous if $v_e(t)$ is not purely sinusoidal.

The simulation parameters are summarized in Table I. The current amplitude $\hat{i}_e$, for the given circuit parameters, is bounded by the maximum current $\hat{i}_{e,max}$. In order not to operate the system at the limit of stability, the maximal amplitude of the current i_e is fixed to 5 A. The path of the control algorithm for an emulated capacitive behavior in the $\Delta\phi_{ei}$-z_{ei}-plane is plotted in **Fig. 8** (blue circles). The end point is given with a larger (red) circle. The phase margin to the unstable area is 15°. The time behavior of the current $i_e(t)$ and the voltage $v_{ei}(t)$ for this case are depicted in **Fig. 9**. The path in the case of an emulated inductive behavior would be similar to the one depicted in Fig. 8 and is hence not shown. The simulations were run in MATLAB/Simulink.

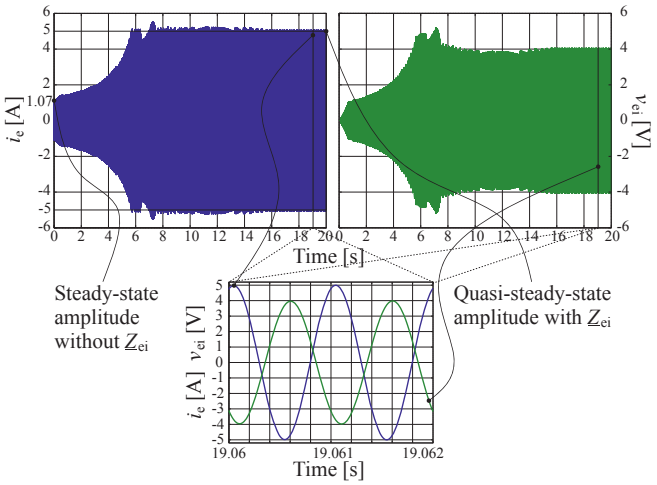

Figure 9: Simulated time behavior of the resonator current $i_e(t)$ [blue] and the ECI voltage $v_{ei}(t)$ [green] for an emulated capacitive behavior [ETSRC according to Fig. 3(a)].

B. Electronically Tuned Parallel Resonant Circuit

The emulated electric capacitive behavior with the ETPRC is depicted in **Fig. 10**. In comparison to the ETSRC, three quantities need to be sensed for the ETPRC instead of two: the resonator current i_e, the excitation voltage v_e and additionally the voltage v_s over the VCCS. The same parameters as for the ETSRC are employed (cf. Table I). As it is shown in Fig. 10, the capacitive behavior can be adjusted exactly, since $\phi_{tot} = -90°$ does not blend along the stability boarder. This represents an advantage over the ETSRC. The drawback, though, is that the $\phi_{tot} = 90°$-line lies in the unstable region. The deviation of the phase ϕ_{tot} to $\pm 90°$ is given by

$$\phi_{dev} = \frac{\pi}{2} - \arctan\left(\frac{\omega_e L_e}{R_e}\right) = 19.48° \qquad (25)$$

for the parameters as given in Table I.

Thus, taking into account a safety margin angle of 15°, it is not possible to evoke an electric inductive behavior with the circuit of Fig. 3(b). To still achieve an inductive behavior the circuit shown in **Fig. 11** can be used. In this case the ECA is modeled by a parallel $R_{ea}L_{ea}$-branch. The characteristics of this circuit are

$$\delta_0 = \frac{1}{2}\frac{L_e L_{ea} + R_e R_{ea} C_e (L_e + L_{ea})}{L_e L_{ea} C_e (R_e + R_{ea})}, \qquad (26)$$

$$\omega_{self} := \sqrt{\omega_0^2 - \delta_0^2} = \sqrt{\frac{R_{ea}(L_e + L_{ea})}{L_e L_{ea} C_e (R_e + R_{ea})} - \delta_0^2}. \qquad (27)$$

The deviation in the phase ϕ_{tot} results to

$$\phi_{dev} = -\left(\frac{\pi}{2} + \arctan\left(-\frac{1}{R_e \omega_e C_e}\right)\right) = -16.29°, \qquad (28)$$

for the circuit in Fig. 11 and the parameters given in Table I.

As demonstrated by the examples, a nearly five times higher current amplitude $\hat{i}_e$ can be reached by actively controlling the resonator with an ECI. In this way, a quality factor of $Q_{dB,t} = 14.0$ dBS is reached (at 1 kHz). Without the electronic

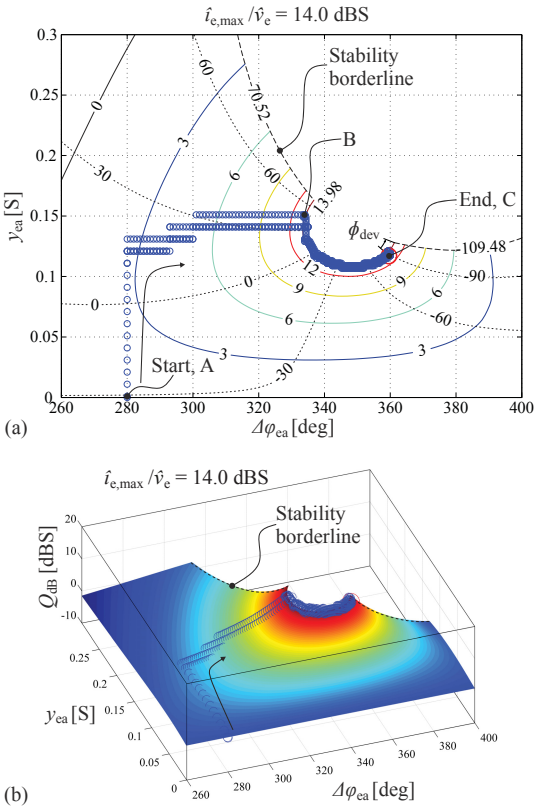

Figure 10: (a) 2D and (b) 3D plot of the control algorithm's path (blue circles) in the $\Delta\varphi_{ea}$-y_{ea}-plane (emulated electric capacitive behavior, ETPRC).

impedance, $Q_{dB,nt} = 0.6$ dBS is obtained. Furthermore, by the same means, the resonant frequency of the resonant circuit could be moved from 1.1 kHz to 1 kHz. Frequency shifts in the other direction and by other amounts are possible as well.

The control algorithm introduced in this paper is fast enough (update rate of 25 ms) to compensate temperature dependent changes of the resistance, which lies in the order of seconds. Also, it can be seen from (10) that with the algorithm shown, the circuit can be adapted to changes in the excitation frequency, as $\phi_{ie} = \omega_e t$ is directly employed to form the voltage $v_{ei}(t)$.

C. Comparison between ETSRC and ETPRC

In this part the advantages and disadvantages of the ETSRC compared to the ETPRC are briefly discussed. On the one hand, it can directly be recognized from Fig. 3 that, compared to the ETSRC, the additional measurement of v_s across the ECI is required for the ETPRC, which adds complexity to the measurement processing unit. On the other hand, a purely inductive or capacitive behavior of the resonant circuit is not adjustable with an ETSRC due to the required stability margins of 15° (cf. Fig. 8). This drawback can be overcome with the ETPRC (cf. Fig. 10). However, two different circuit configurations are necessary: Fig. 3(b) to achieve a purely capacitive behavior and Fig. 11 to adjust a purely inductive

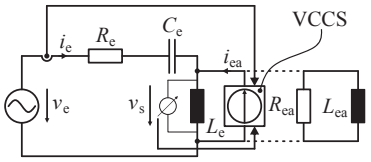

Figure 11: Electronically tuned parallel resonant circuit to emulate an inductive behavior.

behavior. This means that a single circuit configuration is superior to the ETSRC for emulating a capacitive behavior but inferior regarding the inductive behavior or vice versa. Thus, in case the metamaterial should be reconfigurable in order to be employed in different applications, the ETSRC is may still the preferred choice to realize the base units.

Further differences between the ETSRC [cf. Fig. 3(a)] and ETPRC [cf. Fig. 3(b)] exist for the ECI in operation. For the values of the resonant circuit's components and excitation frequency given in Table I and the operating points with $\hat{v}_e = 1$ V, $\hat{i}_e = 5$ A and an arbitrary phase-shift between v_e and i_e (within the stable area including stability limits of 15°), the following can be concluded. The active power generation of the ECI is for the ETSRC and ETPRC equal (same operating point). However, the reactive power absorbed by the ECI is for the ETSRC more than twice as high as for the ETPRC. In the end, the ECI is for the ETPRC exposed to roughly two to four times the voltage stress but to only about one third of the current stress of the ECI for the ETSRC.

Finally, it is noted that the ECI for the ETSRC is a CCVS and for the ETPRC a VCCS. Typically a CCVS can be realized with less hardware efforts than a VCCS, e.g. only a linear power amplifier with additional control logic and measurement processing unit can be employed (cf. Section IV) to emulate the CCVS.

Concluding, the ETSRC compared to the ETPRC requires less hardware efforts, but has potentially a drawback in adjusting a purely capacitive or inductive behavior of the resonant circuit if the metamaterial should not be reconfigurable in its functioning, and its ECI is stressed by twice the reactive power flow. Nevertheless, because of the ETSRC's lower hardware effort and the potential configurability from a capacitive to an inductive behavior, this resonant circuit with corresponding ECI is built as a proof-of-concept prototype and tested as described in the next section.

IV. ECI Prototype and Measurements

The ECI hardware prototype shown in **Fig. 12** was built to experimentally verify the suggested ECI concept and control algorithm. The built circuit is an ETSRC and the prototype's specifications are summarized in Table I. The measured impedance $\underline{Z}_e$ seen by the voltage source v_e with shorted ECI [cf. Fig. 3(a)] is depicted in **Fig. 13**. Including the ECI, based on the measurement, the calculated total impedance $\underline{Z}_{tot}$ of the ETSRC (green, red and magenta lines) is as well shown in the figure for a constant amplitude of the excitation voltage, $\hat{v}_e = 1$ V, and constant phase of $\angle\underline{Z}_{tot} = -75°$ (capacitive behavior). The current amplitude in the green part of $|\underline{Z}_{tot}|$ is

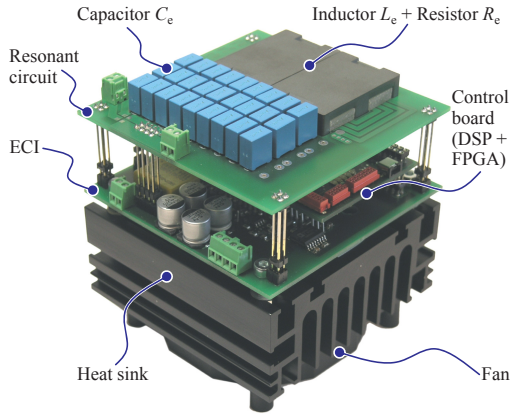

Figure 12: Picture of the electronically controllable impedance (ECI) hardware prototype with a series resonant circuit (ETSRC).

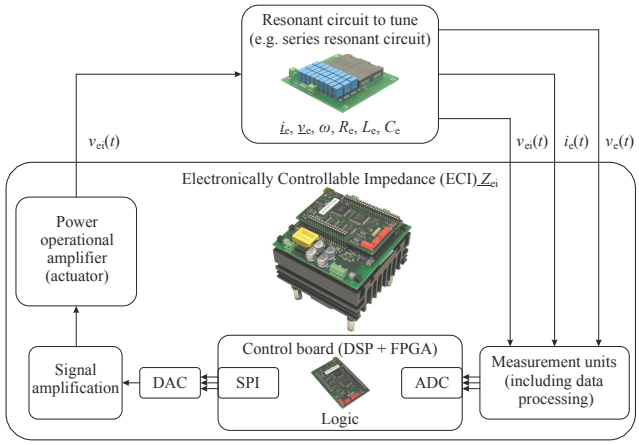

Figure 14: Block diagram of the control of the ECI prototype shown in Fig. 12 (ETSRC).

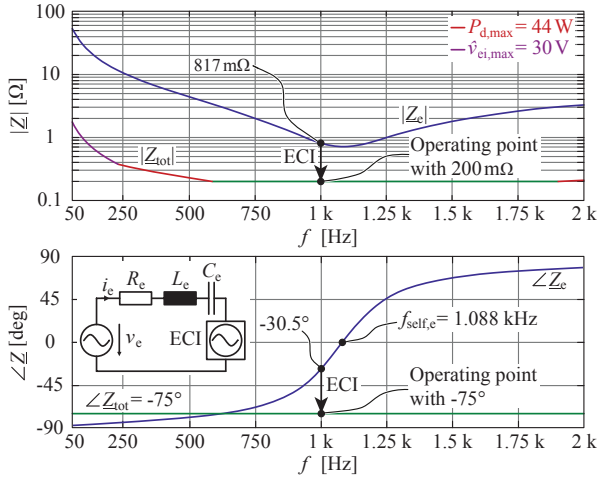

Figure 13: Measured impedance $\underline{Z}_e$ for a shorted ECI (blue line; Agilent 4294A (40 Hz–110 MHz Precision Impedance Analyzer) and based on the measurement calculated total impedance $\underline{Z}_{tot}$ of the ETSRC including the ECI (green, red and magenta lines) for a constant amplitude of the excitation voltage, $\hat{v}_e = 1$ V, and constant phase of $\angle\underline{Z}_{tot} = -75°$ (capacitive behavior). The shift of the operating point achieved with the ECI at 1 kHz is highlighted with arrows.

constantly $\hat{i}_e = 5$ A. In the red and magenta parts, according to the specifications of the hardware prototype given in Table I, $\hat{i}_e$ is reduced due to thermal limitation (max. power dissipation of $P_{d,max} = 44$ W) and maximum voltage across the ECI ($\hat{v}_{ei,max} = 30$ V), respectively.

It can be seen from Fig. 13 that the measured resonant frequency occurs at 1.09 kHz and that the achievable quality factor at the excitation frequency of 1 kHz is $Q_{dB} = 20 \cdot \log_{10}\left(\hat{i}_e/\hat{v}_e\right) = 20 \cdot \log_{10}(1/0.82\ \Omega) = 1.8$ dBS. The purpose of the ECI is to shift the resonant frequency to the excitation frequency and to de-attenuate the resonant circuit as experimentally demonstrated hereinafter.

The power operational amplifier OPA549 from TI/Burr-Brown has been selected to apply the voltage v_{ei} to the series resonant circuit. The heat sink is designed to provide operation up to maximal losses of 44 W in the power operational amplifier (cf. Table I). The control logic is implemented on a TI TMS320F2808 DSP and a Lattice FPGA. A PCB-inductor with an air-gap has been designed for reaching a flat design. Therefore, the resistance R_e is mainly integrated in the inductor. The power operational amplifier is directly mounted on the heat sink. In a next step, the linear amplifier could be replaced by a more efficient switch-mode class D amplifier.

The functional block diagram of the ECI prototype is depicted in **Fig. 14**. The code of the control algorithm (cf. Fig. 7), implemented on the control board, is executed every 10 µs. This includes the reading of the measured quantities from the ADC (Analog to Digital Converter), if necessary updating the electronic impedance values z_{ei} and $\Delta\phi_{ei}$ and applying the new actuator value v_{ei} to the series resonant circuit over the DAC (Digital to Analog Converter - SPI interface) and the amplifiers. In order to protect the ECI, in addition to the current i_e and voltage v_e also the voltages v_{ei} can be monitored. It is noted that the measurement of v_e is only required to determine its phase with respect to the current i_e. A more detailed hardware realization of the ECI is shown in **Fig. 15**, from where the different components belonging to the functional blocks in Fig. 14 can be identified.

The measured path of the control algorithm (blue circles), which confirms the simulated one, is presented in **Fig. 16**. The waveforms over time at the start (A) and end point (C) of the algorithm's path are shown in the figure as well. The ECI, especially the power operational amplifier, is supplied by ±12 V from the switched SW5250A source from Elgar. The excitation voltage $v_e(t)$ is generated by the linear 4-quadrant amplifier PAS1000 from Spitzenberger&Spies.

Considering the measurements, two effects have to be shortly discussed. Firstly, the values of the inductance L_e[1] and resistance R_e increase with temperature and thus with

[1]The core material of L_e is EPCOS' N87, which shows an increasing permeability with temperature ($< 200°$C). Accordingly, the value of L_e is augmenting with temperature.

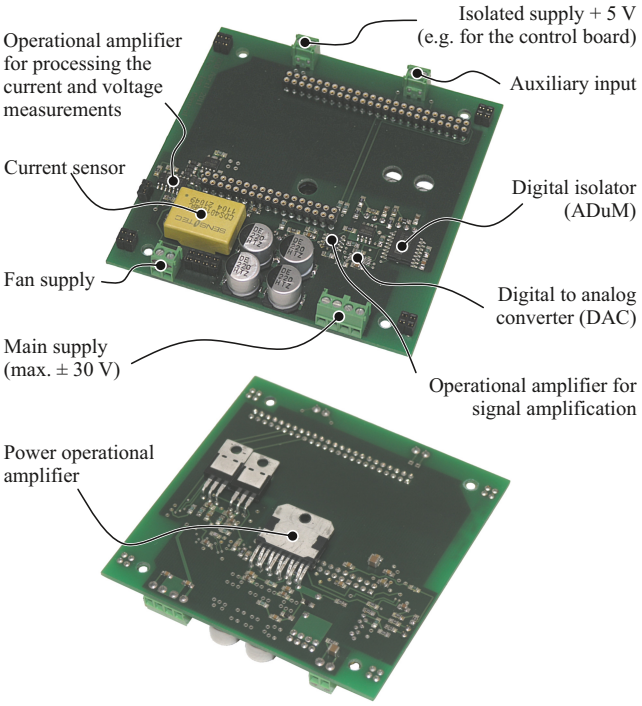

Figure 15: Top and bottom views of the ECI without heat sink and control board to identifying the different components (cf. Fig 14, ETSRC).

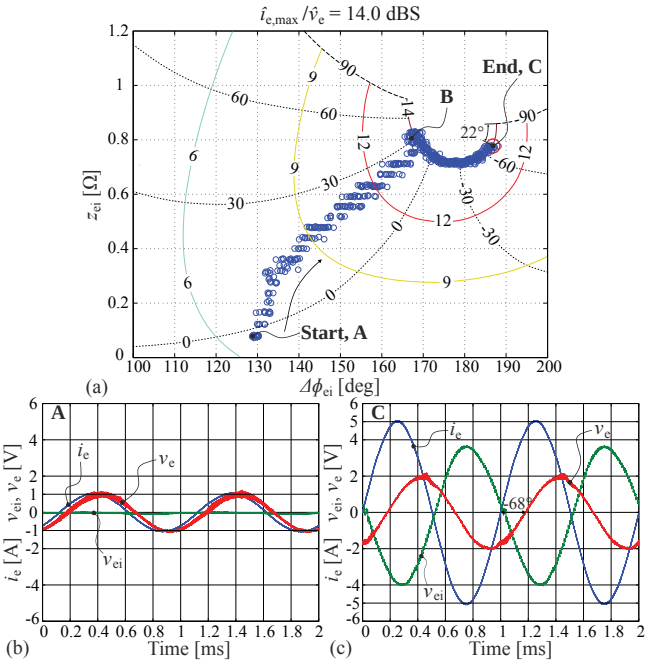

Figure 16: (a) Measured path of the control algorithm in the $\Delta\phi_{ei}$-z_{ei}-plane; resonator current $i_e(t)$ [blue], ECI voltage $v_{ei}(t)$ [green] as well as excitation voltage $v_e(t)$ [red] at (b) the start and (c) the end point for an emulated capacitive behavior (ETSRC).

the current amplitude $\hat{i}_e$. For the waveforms at point (C), the estimated resistance is $R_e = 0.91\ \Omega$ and the estimated inductance is $L_e = 394\ \mu H$. Secondly, the amplitude of the excitation voltage v_e varies dependent on the total impedance $\underline{Z}_{tot}$. The more inductive the total impedance $\underline{Z}_{tot}$ is, the more the voltage amplitude drops and on the other side, the more capacitive the impedance is, the more the voltage is boosted. As a result, the voltage amplitude $\hat{v}_e(t)$, initially 1.0 V, first decreases to increase later on, and to reach 1.9 V at point C. Because the amplitude of the excitation voltage influences the trajectory of the equiquality-lines and of the phase ϕ_{tot} (of the total impedance $\underline{Z}_{tot}$) in the $\Delta\phi_{ei}$-z_{ei}-plane, the equiquality-lines and ϕ_{tot} vary with time. This effect is more dominant than the one resulting from the temperature induced changes of the circuit components. In conclusion, the equiquality-lines and the phase ϕ_{tot} depicted in **Fig. 16** are exemplary and combine the trajectories over time into one representative trajectory.

Despite the mentioned second point, the measurements confirm the simulations and the theoretical analysis to evoke a capacitive or an inductive behavior with a ETSRC (or ETPRC). In addition, they prove that the ECI's control algorithm can cope with varying parameters. Furthermore, by measurements introduced errors in the resulting ECI amplitude z_{ei} and phase $\Delta\phi_{ei}$ are automatically compensated by the control algorithm.

The higher the frequency shift from f_{self} to f_e is, the greater the voltage v_{ei} becomes. Thus, in order not to exceed the maximal allowable voltage $\hat{v}_{ei,max} = 30$ V, the maximum frequency shift is limited. With the values of the resistance and inductance given in Table I, the maximal self-resonant frequency f_{self} of the circuit in Fig. 3(a) is 1.91 kHz for an emulated capacitive and 1.88 kHz for a inductive behavior. The corresponding minimal frequency is 266 Hz for both cases.

V. Conclusion

In this paper an active base unit and / or active metamaterial for shielding of magnetic stray fields at low- and medium-frequencies is conceptualized, designed and tested. Such an active metamaterial is assembled by an array of engineered active base units, each one containing a LCR-resonator and a control unit called electronically controllable impedance (ECI). The inductor of the resonator is formed by a conductive structure generating a magnetic field. The LCR-resonant circuit together with the ECI builds then an electronically tuned series or parallel resonant circuit (ETSRC or ETPRC). The disadvantages of a passive metamaterial, which are the deterioration of the screening factor by component value tolerances and variations with temperature and / or by aging, can be overcome with an active metamaterial.

An ECI consists of a 4-quadrant power converter with integrated measurement and control units for emulating an impedance in all four quadrants of the complex impedance plane. The current (or voltage) is measured and the voltage (or current) is outputted by the power converter according to an implemented control strategy. First, the ECI evokes ideally a purely capacitive or inductive behavior of the ETSRC or ETPRC by tuning the resonant frequency of the resonator

to a frequency slightly lower or higher than the excitation frequency. And second, it adjusts a desired high quality factor Q_{dB}.

A control algorithm was designed and implemented in MATLAB/Simulink, which finds the operation points with the highest quality factor, under given voltage and current limitations. It further adjusts a capacitive or inductive behavior of the circuit, regardless whether the circuit parameters are exactly known or not.

An ETSRC hardware prototype was built with a power operational amplifier as current controlled voltage source (CCVS) and the control algorithm was implemented on a DSP+FPGA to verify the proposed concept for the ECI. It is demonstrated that an actively controlled resonator exhibits a nearly five times higher current amplitude and that the resonant frequency of the resonant circuit could be shifted from $1.1\ \mathrm{kHz}$ to $1\ \mathrm{kHz}$. The quality factor Q_{dB} could be increased from $0.6\ \mathrm{dBS}$ to $14.0\ \mathrm{dBS}$. The experimental results confirm the simulations and thus the concept to emulate a capacitive behavior with the ETSRC.

ACKNOWLEDGMENT

The authors would like to thank Christian Hafner from the Electromagnetic Fields and Microwave Electronics Laboratory (IFH, ETH Zurich) for the introduction to the properties of metamaterials and interesting related discussions.

REFERENCES

[1] V. Veselago, L. Braginsky, V. Shklover, and C. Hafner, "Negative refraction index materials," *Journal of Computational and Theoretical Nanoscience*, vol. 3, no. 2, pp. 1–30, 2006.

[2] P. Alitalo and S. Tretyakov, "Electromagnetic cloaking with metamaterials," *Elsevier Ltd., Materialstoday*, vol. 12, no. 3, pp. 22–29, 2009.

[3] C. Caloz, "Perspectives on em metamaterials," *Elsevier Ltd., Materialstoday*, vol. 12, no. 3, pp. 12–20, 2009.

[4] D. R. Smith, W. J. Padella, D. C. Vier, S. C. Nemat-Nasser, and S. Schultz, "Composite medium with simultaneously negative permeability and permittivity," *Physical Review Letters*, vol. 84, no. 18, pp. 4184–4187, 2000.

[5] G. V. Eleftheriades and K. G. Balmain, Eds., *Negative-Refraction Metamaterials, Fundamental Principles and Applications*. IEEE Press, Wiley InterScience, 418 p., 2005.

[6] J. B. Pendry, A. J. Holden, D. J. Robbins, and W. J. Stewart, "Magnetism from conductors and enhanced nonlinear phenomena," *IEEE Trans. Microw. Theory Tech.*, vol. 47, no. 11, pp. 2075–2084, 1999.

[7] M. Choi, S. H. Lee, Y. Kim, S. B. Kang, J. Shin, M. H. Kwak, K.-Y. Kang, Y.-H. Lee, N. Park, and B. Min, "A terahertz metamaterial with unnaturally high refractive index," *Nature Research Letter*, vol. 470, pp. 369–374, 2011.

[8] B. Wang, W. Yerazunis, and K. H. Teo, "Wireless power transfer: Metamaterials and array of coupled resonators," *IEEE Proc.*, vol. 101, no. 6, pp. 1359–1368, 2013.

[9] T. Steinmetz and J. Smajic, *Magnetic stray field analysis of dry-type transformers - Simulation vs. measurement*. Presentation, ABB Switzerland Ltd., Corporate Research, 26 p., 2010.

[10] J. Smajic, T. Steinmetz, B. Cranganu-Cretu, A. Nogues, R. Murillo, and J. Tepper, "Analysis of near and far stray magnetic fields of dry-type transformers: 3-d simulations versus measurements," *IEEE Trans. Magn.*, vol. 47, no. 5, pp. 1374–1377, 2011.

[11] M. Boyvat, "Low frequency magnetic metamaterials and wireless control of forces and torques," Ph.D. dissertation, ETH Zurich, 2013, 116 p.

[12] H. Moon, S. Kim, H. H. Park, and S. Ahn, "Design of a resonant reactive shield with double coils and a phase shifter for wireless charging of electric vehicles," *IEEE Trans. Mag.*, vol. 51, no. 3, pp. 1–4, 2015.

[13] B. Hofmann, "Distribution transformers and emc," *Siemens, Special Reprint*, 8 p., 2009.

[14] R. Bosshard, "Multi-objective optimization of inductive power transfer systems for EV charging," Ph.D. dissertation, ETH Zurich, 2015, 251 p.

[15] P. L. Sergeant, L. R. Dupre, M. D. Wulf, and J. A. A. Melkebeek, "Optimizing active and passive magnetic shields in induction heating by a genetic algorithm," *IEEE Trans. Mag.*, vol. 39, no. 6, pp. 3486–3496, 2003.

[16] G. Lipworth, J. Ensworth, K. Seetharam, J. S. Lee, P. Schmalenberg, T. Nomura, M. S. Reynolds, D. R. Smith, and Y. Urzhumov, "Quasi-static magnetic field shielding using longitudinal mu-near-zero metamaterials," *Sci. Rep. 5, 12764*, pp. 1–8, 2015.

[17] D. O. Boillat, T. Friedli, and J. W. Kolar, "Electronically controllable impedance for tuning of active metamaterials," in *37th Annual Conf. on IEEE Industr. Electron. Soc. (IECON)*, 2011, pp. 1335–1341.